Proceedings of ASME Turbo Expo 2025
Turbomachinery Technical Conference and Exposition
GT2025
June 16-20, 2025, Memphis, Tennessee

GT2025-153718

ON THE UNSTEADY BEHAVIOUR OF A LIQUID HYDROGEN FUEL SYSTEM PUMP FOR AIRCRAFT ENGINE APPLICATIONS

Dimitrios Lamprakis[1,*], David John Rajendran[1], Martin Yates[2], Ioannis Roumeliotis[1], Vassilios Pachidis[1]

[1]Rolls-Royce University Technology Centre, Cranfield University, MK43 0AL, United Kingdom
[2]Rolls Royce plc., Birmingham Business Park, Birmingham, B37 7YP, United Kingdom

ABSTRACT

The unsteady behaviour of a 2-stage liquid hydrogen (LH2) fuel system pump for future aircraft engine applications is investigated herein by means of full wheel, uRANS simulations. Compressibility, thermodynamic state and leakage flow effects are investigated to assess their individual contribution in the stability and unsteady pump operation. This is achieved by comparing three pump configurations along with two different modelling approaches: a baseline geometry without cavities, one with shroud cavities only, and a full model comprising all cavities, while real gas and constant property fluids are used to assess compressibility effects. An initial performance and component stability analysis is carried out using steady-state simulations and standard non-dimensional quantities. Unsteady simulations are subsequently performed combining the different modelling approaches and geometries at very low, off-design flow rates, representative of part-load operation. Unsteady signals are recorded at several planes in the pump flow path along with multiple monitor points around the annulus. These are then analysed in the frequency domain, providing a link between key flow features and the high-power frequency content. Compressibility effects are shown to slightly penalise the head rise of the pump without however penalising stability. The implications of the thermodynamic state of hydrogen on the transient pump response are minor, while the recorded head fluctuation amplitude of the baseline configuration reaches 18.4% of the mean value. Both impellers of the baseline configuration exhibit a mild surge-type of behaviour associated with stalled flow-induced blockage near the volute tongue resulting in heavy stalling of the splitter blades. Leakage flows negatively affect the steady-state pump performance but alleviate full and splitter blade stall, reducing the pump's oscillation intensity by 30.6% through partial suppression of the stalled flow near the volute tongue. The study highlights the importance of transient performance in low-specific-speed hydrogen fuel pumps, as part-load operation may entail significant operability challenges.

*Corresponding author: Dimitrios.Lamprakis@cranfield.ac.uk

Keywords: Pump, Aircraft, Hydrogen, Leakage, Head, uRANS, Instability, Stall, Surge

NOMENCLATURE

Roman letters

C_p	Static pressure recovery coefficient
D	Diameter
$\widetilde{E}$	Signal energy
f	Frequency
f_1	Fundamental frequency
f_B	Blade passing frequency
f_s	Sampling frequency
f_Ω	Rotor frequency
g	Gravitational acceleration
H	Head
$\dot{m}$	Mass flow
N	Rotational speed
N_s	Number of samples
P	Static pressure
P_0	Stagnation pressure
Q	Volumetric flow rate
t	Time
U_{tip}	Tip speed
$\widetilde{P}$	Signal power
W	Relative velocity magnitude
X	Fourier coefficient

Greek letters

β	Relative flow angle
θ	Circumferential position
Λ	Generic scalar quantity
$\overline{\Lambda}$	Averaged generic scalar quantity
Λ'	Fluctuating component of a generic quantity
ρ	Density
ϕ	Flow coefficient

Copyright © 2025 by Rolls-Royce plc;
reuse license CC-BY 4.0

ψ Head rise coefficient
ω Angular velocity

Subscripts
d Design conditions
imp Impeller property
in Inlet property
$norm$ Normalised property
out Outlet property
tt Total-to-total property
ts Total-to-static property
vol Volute property
$*$ Modified property

Abbreviations
CFD Computation fluid dynamics
DP Design point
HP High-pressure
LE Leading edge
$LH2$ Liquid hydrogen
LP Low-pressure
NL No leakage
PSD Power spectral density
RGP Real gas property
RMS Root mean square
TE Trailing edge
$(U)RANS$ (Unsteady) Reynolds-averaged Navier-Stokes
WL With leakage

1. INTRODUCTION

Amongst the different technologies aiming to decarbonise the aviation industry, liquid hydrogen (LH2) constitutes one of the promising ones, due to its high mass energy density and zero carbon content [1–3]. Safe and reliable implementation of LH2 in the aircraft poses several challenges as its on-board storage in liquid form requires cryogenic temperatures which entail a series of design, structural and safety challenges [4]. In addition to these challenges, the successful implementation of LH2 in aircraft is dependent on the design of a reliable and efficient LH2 fuel system.

The LH2 fuel system pre-conditions the fuel by heating and pressurizing it to meet engine combustor requirements. This involves raising the temperature from 20 K (cryogenic storage) to 300 K and the pressure from 1–3 bar (tank storage) to 50 bar (combustor delivery) [5]. For efficiency, the LH2 is pressurized as a liquid and heated only after reaching a supercritical state. Pressurization is achieved through a low-pressure booster pump and a high-pressure (HP) pump. The booster pump transfers the fuel from the cryogenic tank while keeping it sub-cooled for the HP pump. The HP pump raises the fuel pressure to the required delivery conditions based on the mission profile, ensuring it reaches the combustor at the required pressure under varying conditions [6, 7]. Centrifugal pumps are preferred for their higher pressure rise in a smaller, lighter design compared to positive displacement pumps used in conventional aviation fuels. Centrifugal pumps for LH2 have been primarily used in space applications and niche nuclear cooling systems. In rocket engines, these HP pumps are typically multi-stage centrifugal turbopumps, driven by a turbine and are designed for high specific speeds due to the larger mass flow rates compared to aircraft applications. These pumps operate mostly near design conditions and are intended for single-mission use [8–10]. On the contrary, aircraft engine HP pumps are required to operate at a wider operating envelope e.g. take-off, cruise, idle, while ensuring reliability and long life expectancy. Aircraft fuel systems also handle lower mass flow rates, resulting in low-specific-speed pumps, a regime where LH2 centrifugal pumping remains underexplored. Detailed investigations into LH2 pumping characteristics are essential for fuel system design during preliminary engine cycle studies. Understanding the dynamic response of the LH2 fuel system at different operating conditions is essential and inextricably linked to the HP pump response. This has not been investigated and reported before in the literature. Investigations into such unsteadiness is necessary to ascertain the safe operating combinations of flow rates and rotational speeds of the HP pump.

Several studies on the onset and development of instabilities in turbomachinery have been performed, but the underlying mechanisms are still to this day not fully understood, while the knowledge gap is wider when considering centrifugal turbomachines [11]. Spakovszky and Roduner [12] experimentally investigated the stall inception mechanisms of a centrifugal compressor with and without bleed flow downstream of the impeller outlet, capturing spike and modal wave stall inception. In a similar study [13], utilising numerical simulations of an isolated diffuser model, spike stall inception was demonstrated to be associated with spanwise non-uniformity of the flow, while modal waves with impeller-diffuser interaction. Rotating stall in impellers, vaneless and vaned diffusers is reported by Braumbusshe [14]. Fringe et al. [15] report mild, progressive and abrupt rotating impeller stall in an impeller-vaneless diffuser experimental configuration, reporting velocity fluctuations up to 30% of the mean value for the latter. The volute inlet flow angle was identified as the critical parameter dictating the type of rotating stall and its pattern. Shim and Kim [16] numerically investigated the instability mechanisms of a pump with volute. Flow instability in the volute was triggered by the radial pressure gradient near the volute tongue and the circumferential pressure gradient along the volute passage, with suction recirculation appearing upstream of the impeller at partial flow conditions. The onset of instability correlated with a change in the sign of the volute C_p curve slope, making it a key predictor. Wang and Tsukamoto [17] investigated the unsteady behaviour of a centrifugal pump with vaned diffuser at part-load operation. The impeller blade passing frequency was identified as the dominant pressure fluctuation across all flow rates due to rotor-stator interaction. Dominant, low-frequencies downstream of the impeller are reported, associated with flow separations, rotating stall, and reverse flow. Unstable operation at lower flow rates was mainly linked to flow separations and stall in the diffuser. In the mid and higher part-load range, unsteadiness was linked to both impeller and diffuser stall, with the former being the dominant in the higher part-load range due to a separation bubble at the impeller pressure side. The impeller - volute tongue interaction at part-load operation has been identified in several studies as one of the primary sources linked to pres-

Copyright © 2025 by Rolls-Royce plc;
reuse license CC-BY 4.0

sure oscillations in both low and high-specific speed centrifugal pumps [18, 19]. Kaupert and Staubli [19] report progressively increasing pressure fluctuations in an experimental study with an impeller-double spiral volute configuration, reaching 35% of the mean pump head at the lowest flow rate. These significantly influence the impeller pressure-field during the entire off-design operation. Casimir et al. [20] report asymmetric impeller loading during part-load operation, driven by backflow and jet formation within the passages. This effect is further exacerbated by the development of a vortex near the lower volute tongue, which heavily affects the adjacent passage, disrupting local pressurization and causing instantaneous negative loading.

This study aims to provide insights into the unsteady response and primary driving flow mechanisms of a 2-stage, centrifugal pump design, representative of future LH2 aircraft fuel systems. Three pump configurations are employed: a baseline without cavities, one with only shroud leakage cavities and the complete configuration with the entire cavity network including motor cavities. Real gas and constant properties are implemented to model hydrogen. Combining the different configurations, modelling approaches and comparing steady-state and transient data, the stability and transient response of the pump at low, off-design flow rates is analysed. Further analysis is carried out at a component level, using non-dimensional performance quantities and Fourier transformations to extract the frequency content. These are then linked to flow-field features. Understanding the unsteadiness of these pumps and the underpinning mechanisms is essential in terms of design and overall fuel system performance, as aircraft pumps are expected to operate at a wide range of off-design conditions. Their unsteady operation is critical for the safe and reliable operation of future low carbon propulsion systems, aiming to decarbonise aviation industry.

2. COMPUTATIONAL DOMAIN AND MODELLING METHOD

The pump investigated herein is a 2-stage centrifugal design, representative of a high-pressure, LH2 pump for future aircraft engine fuel systems. Pressurisation is achieved through 2 identical radial impeller stages in series, with the first being preceded by an inducer. The flow is then further diffused in the volutes and a downstream diffusing duct. The two stages are connected via a 180^0 bend, linking the diffusing duct of the former with the inlet of the latter. Details on the pump geometry are provided in [21]. The pump is considered to be electrically driven by a motor. The pressurisation of hydrogen is sufficiently high to precipitate a change in the thermodynamic state of hydrogen, from saturated liquid at the inlet, to supercritical at the outlet of the last pump unit.

2.1 MODELLING APPROACH

To numerically investigate the stability and transient characteristics of the pump and individually assess the implications of compressibility and leakage flow effects, three pump configurations are investigated with different numerical approaches, shown in Fig. 1. The first (baseline), comprises all principal flow paths and turbomachinery components without leakage cavities. The second one, is identical to the baseline model with the inclusion of the impeller shroud cavities and is used for the unsteady simulations. The third configuration is the full geometry, incorporating all leakage cavities and is used in steady-state simulations. The hub and motor cavities of the detailed pump model are omitted in the unsteady simulations since they exhibit negligible interaction with the main flow path, as the momentum and pressure forces reach an equilibrium shortly after these fill with hydrogen. The shroud cavities however, enable recirculation of large amounts of flow from the outlet to the inlet of the impeller introducing significant head and efficiency penalties [21]. The first two configurations are thereby sufficient for the assessment of leakage flow effects on the unsteady characteristics of the pump, while preserving computational requirements within reasonable margins.

Compressibility effects are not expected to be negligible, as a density drop of around 10% from the inlet to the outlet was recorded at design conditions [21]. To dissect compressibility effects from other inherent mechanisms triggering unsteadiness in the pump's operation, two modelling approaches are adopted: a constant-property and a real gas property (RGP) modelling approach. The first assumes constant properties taken at inlet conditions from REFPROP [22], while the latter utilises RGP tables from REFPROP's database containing all necessary thermodynamic properties at various pressures and temperatures within a prescribed range.

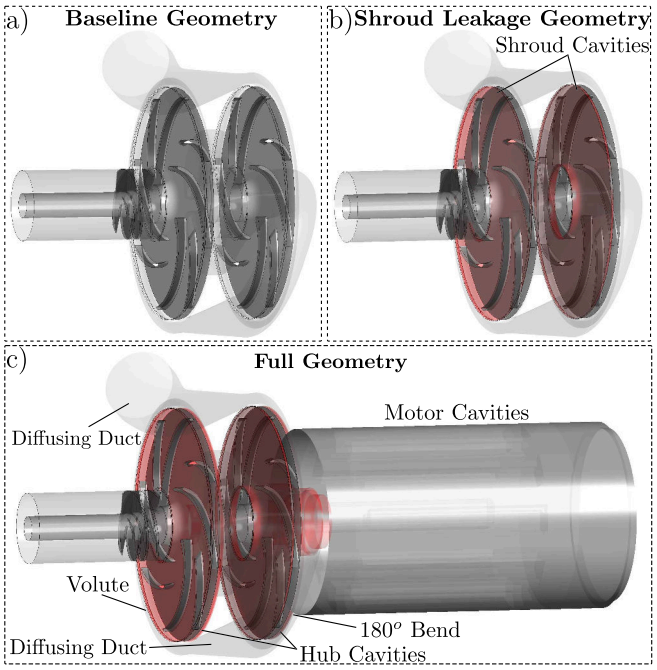

FIGURE 1: OVERVIEW OF A) BASELINE, B) SHROUD LEAKAGE AND C) FULL PUMP CONFIGURATIONS.

2.2 GRID AND BOUNDARY CONDITIONS

Full-wheel, unsteady, Reynolds-Averaged, Navier-Stokes (uRANS) simulations are carried out in a computational domain combining structured (turbo components) and unstructured (volutes, ducts and leakage cavities) grids, generated in ANSYS® TurboGrid™and ANSYS® Meshing™, respectively.

Copyright © 2025 by Rolls-Royce plc;
reuse license CC-BY 4.0

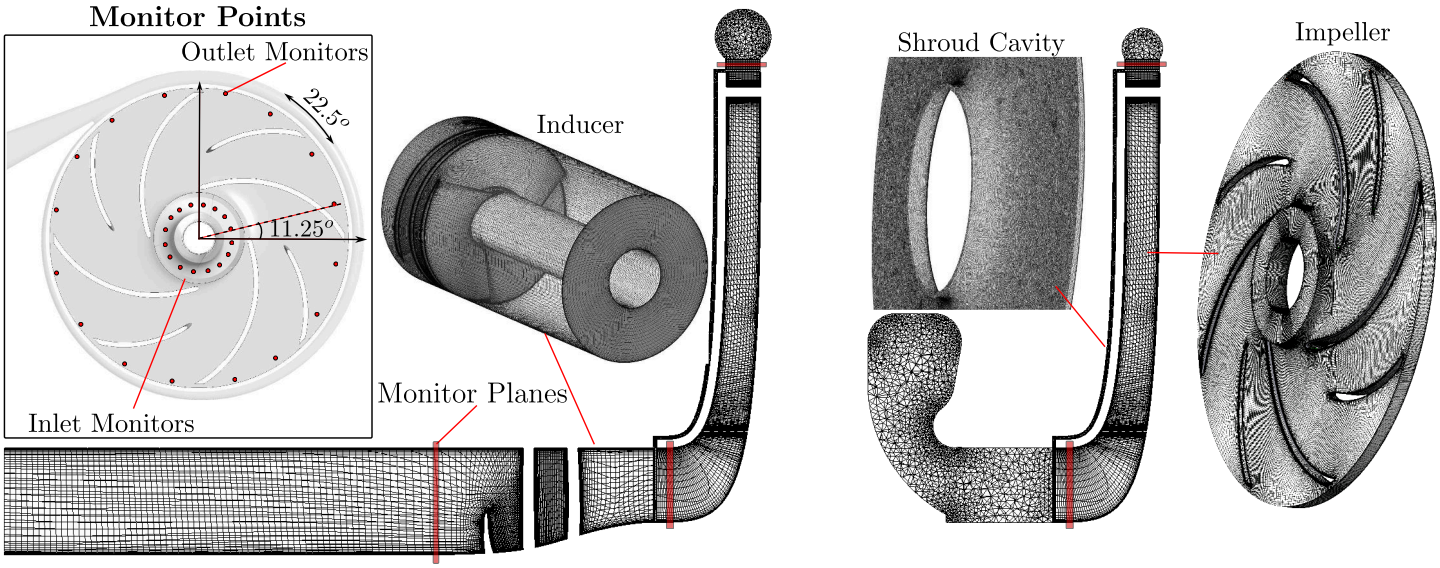

FIGURE 2: INDUCER, IMPELLER AND MERIDIONAL, CROSS-SECTIONAL VIEW OF THE COMPUTATIONAL DOMAIN CORRESPONDING TO THE SHROUD LEAKAGE PUMP CONFIGURATION. THE CIRCUMFERENTIAL POSITION OF THE MONITOR POINTS AT THE IMPELLER OUTLET (LEFT) ALONG WITH THE POSITION OF THE MONITOR PLANES ARE ALSO SHOWN.

The turbomachinery components are discretised with approximately 12.9×10^6 elements. The volutes along with the adjacent ducting components and shroud leakage cavities are discretised with 15.9×10^6 elements. This translates to a total count of approximately 18.7×10^6 elements for the baseline, and 34.7×10^6 and 78.8×10^6 elements for the shroud leakage and full configuration, respectively. Near-wall grid refinements are carried out in turbomachinery components only, while the shroud leakage cavities are resolved with a fine mesh to preserve grid metrics within reasonable limits. A meridional cross-sectional view of the shroud leakage pump configuration along with an overview of the inducer, impeller and shroud leakage cavity meshes are shown in Fig. 2.

The flow-field solution is obtained using ANSYS® CFX™solver. Stagnation pressure and temperature are imposed at the inlet, while mass flow is imposed at the outlet. For very low flow operation, the pressure inlet boundary condition was replaced with an opening, allowing inflow and outflow to assist convergence. The working fluid is hydrogen and is modelled either as a constant property liquid/supercritical fluid, depending on the pump stage under consideration, or as a real gas using RGP tables. These contain thermodynamic properties of both liquid and gaseous phase enabling locally the flow to change state without however accounting for the associated energy required for the phase transition. The $k-\omega$ *SST* turbulence model is preferred due to its better performance in turbomachinery and separated flows (see [23]) and its application in relevant LH2 applications [24]. The energy equation is activated. For steady-state simulations, frozen rotor interfaces are numerically adjoining rotating and stationary domains, while transient rotor stator interfaces (rotating mesh) are used for transient simulations. All walls are considered adiabatic with no-slip condition. Higher-order schemes are used to resolve advection and turbulence terms along with the second-order backward Euler time-stepping scheme for transient terms. All simulations are single phase and carried out in the full annulus geometry.

2.3 PERFORMANCE METRICS

The instantaneous response of the individual components and the entire pump is recorded at each timestep by extracting pitchwise-averaged properties at the inlet and outlet of the inducer, the impellers and the pumps (see Fig. 2). Additional transient flow-field data are recorded at 16 circumferential, evenly spaced locations at the inlet and outlet of the turbomachinery components. These aim to capture the existence of any potential disturbances that might be associated with the unsteadiness exhibited by the individual components. The circumferential recordings would also enable the identification of any potential rotating stall cells travelling at a fraction of the rotor speed. The volumetric flow rate, flow coefficient, total-to-total head rise and head rise coefficient are given by Eqns.(1)-(4):

$$Q_{in} = \frac{\dot{m}_{in}}{\rho_{avg}} \tag{1}$$

$$\phi = \frac{Q}{ND^3} \tag{2}$$

$$\Delta H_{tt} = \frac{\Delta P_{tt}}{\rho_{avg} g} \tag{3}$$

$$\psi_{tt} = \frac{g \Delta H_{tt}}{N^2 D^2} \tag{4}$$

In the above equations, the average density is the arithmetic average of the inlet and outlet density of the component under consideration, i.e. $\rho_{avg} = 0.5(\rho_{in} + \rho_{out})$. Additional non-dimensional quantities are subsequently utilised to assess the performance of the volutes and turbomachinery components: total-to-static head rise coefficient, ψ_{ts}, as well as standard and modified static pressure recovery coefficients, C_p and C_{p*} respectively. The latter

Copyright © 2025 by Rolls-Royce plc;
reuse license CC-BY 4.0

normalisation is preferred in the unsteady data analysis as it dissects the static pressure variations from the variations of the inlet dynamic head. The quantities are defined as per Eqns. (5) - (7).

$$\psi_{ts} = \frac{P_{out} - P_{0,in}}{\rho_{avg} N^2 D_{tip}^2} \tag{5}$$

$$C_p^{vol} = \frac{P_{out} - P_{in}}{P_{0,in} - P_{in}} \tag{6}$$

$$C_{p*}^{vol} = \frac{P_{out} - P_{in}}{0.5\rho U_{tip}^2} \tag{7}$$

The analysis of the time-dependent signals is performed primarily in the frequency domain. The signals are transformed from the time domain to the frequency domain using fast Fourier transformation (FFT) and analysed within time frames corresponding to the last 10-15 revolutions. The first few revolutions are always excluded from the dataset to remove the effect of the initial transient phenomena related to the change in the boundary conditions. For one-sided FFT analysis, the energy, power and power density (PSD) of the signals in the frequency domain are given by [25, 26]:

$$\widetilde{E} = 2\int_0^\infty \left(\frac{|X(f)|}{N_s}\right)^2 df \tag{8}$$

$$\widetilde{P} = 2\frac{f_s}{N_s}\int_0^\infty \left(\frac{|X(f)|}{N_s}\right)^2 df \tag{9}$$

$$PSD = 2\frac{f_s}{N_s}\left(\frac{|X(f)|}{N_s}\right)^2 \tag{10}$$

, where $X(f)$ the Fourier coefficients, f the frequency, f_s the sampling frequency and N_s the number of samples.

2.4 PERFORMANCE METRICS

To quantify the errors associated with the spatial resolution, a grid convergence analysis has been carried out on a component level, i.e. inducer, impellers and volutes, the details of which can be found in [21]. The medium grid was chosen for all components, as the head rise/loss errors with respect to the Richardson extrapolated values did not exceed 1.01% and 2.82% for the turbomachinery components and the volutes, respectively. To ensure that the resolved timescales are sufficient to capture the primary transient flow features, the unsteady behaviour of the impellers and the pump is obtained and analysed using three different timesteps: $\Delta t_1 = 1e-05$, $\Delta t_2 = 1.5e-05$ and $\Delta t_3 = 2.5e-05$. Simple multiples for the variation of all timesteps were avoided to mitigate the potential of aliasing, resonance, patterned error accumulation or filtering out/amplifying certain transient features.

Figure 3 shows the first and second stage impeller as well as the overall pump head coefficient within a window corresponding to the last 8 recorded revolutions. The plotted signals are low-pass filtered for better clarity. The time-averaged mean values of the different signals are also shown, constituting a primary quantity to assess the effect of the timestep on the unsteady pump behaviour. These exhibit a notable difference in both impeller stages for the largest timestep, up to 7% for the first stage, while the difference between the two smallest timesteps does not exceed 0.95%. At a pump level, the discrepancies diminish markedly and are rather negligible.

TABLE 1: NORMALISED FIRST, SECOND STAGE AND PUMP RMS HEAD COEFFICIENT FLUCTUATIONS.

Δt [μs]	$\Delta t/\Delta t_s$	$\psi'_{rms}/\overline{\psi}\|_{imp1}$	$\psi'_{rms}/\overline{\psi}\|_{imp2}$	$\psi'_{rms}/\overline{\psi}\|_{pump}$
10	2/3	7.08	10.278	7.17
15	**1**	**7.55**	**9.82**	**7.28**
25	5/3	8.02	9.58	6.68

To further assess the impact of the timestep, the intensity of the fluctuations is compared, expressed via their root mean square (RMS) value. These are computed following Eqns. (11) - (12), where Λ a generic scalar quantity.

$$\overline{\Lambda'} = \frac{\int_{t1}^{t2}(\Lambda - \overline{\Lambda})dt}{\Delta t} \tag{11}$$

$$\Lambda'_{rms} = \sqrt{\frac{\int_{t1}^{t2}(\Lambda')^2)dt}{\Delta t}} \approx \sqrt{\sum_{k=k_1}^{k_2}\frac{\Lambda'^2}{N_s}} \tag{12}$$

Table 1 summarises the RMS head coefficient fluctuations, normalised with the corresponding time-averaged values, annotated in Fig. 3. The line with the bold letters corresponds to the values obtained with the adopted timestep, Δt_s. This was deemed an appropriate compromise as the discrepancy from the smallest timestep both in terms of average and fluctuating properties is within reasonable limits.

3. PUMP STABILITY ANALYSIS

Prior to the characterisation of the pump's unsteady response, the steady-state behaviour is investigated by analysing non-dimensional performance metrics at a component and overall pump level. This enables the identification of the critical components, from which instabilities and unsteadiness might be originating from, while allowing for a hierarchy of the effects of compressibility, leakage, and the fluid's thermodynamic state based on their anticipated impact on the pump's unsteady response.

The effect of compressibility, leakage flows and thermodynamic state are assessed by comparing different modelling approaches and pump configurations. All steady-state simulations are carried out with the full and baseline geometries, depicted in Fig. 1a,c. To identify signs indicative of potential pump and component instabilities, a similar approach to that of Spakovszky and Roduner [12] and Everitt and Spakovszky [13] is adopted. While the analysis was performed in a centrifugal compressor with vaned diffuser, its applicability to pumps with vaneless diffuser was also demonstrated [16]. The gradient of the pump's total-to-total and total-to-static head rise coefficients are plotted in Fig. 4a-c, with the gradient of the former typically being more indicative of the component's performance and the latter of the component's stability. In pumps, however, these tend to be

Copyright © 2025 by Rolls-Royce plc;
reuse license CC-BY 4.0

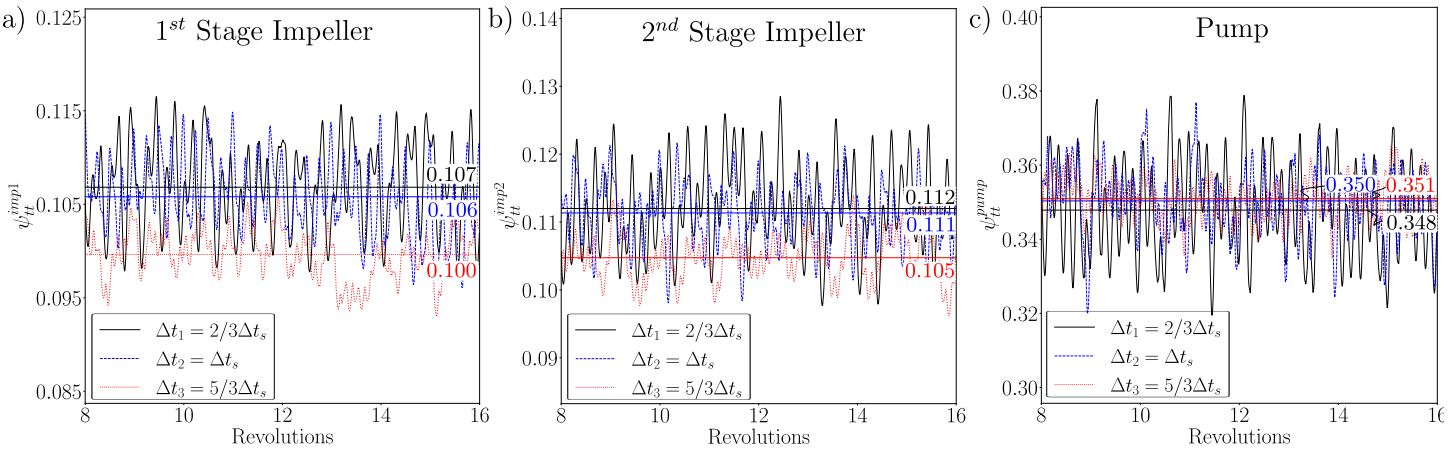

FIGURE 3: FILTERED INSTANTANEOUS AND MEAN HEAD RISE COEFFICIENT RECORDINGS OF A) FIRST STAGE IMPELLER, B) SECOND STAGE IMPELLER AND C) PUMP FOR 3 DIFFERENT TIMESTEPS.

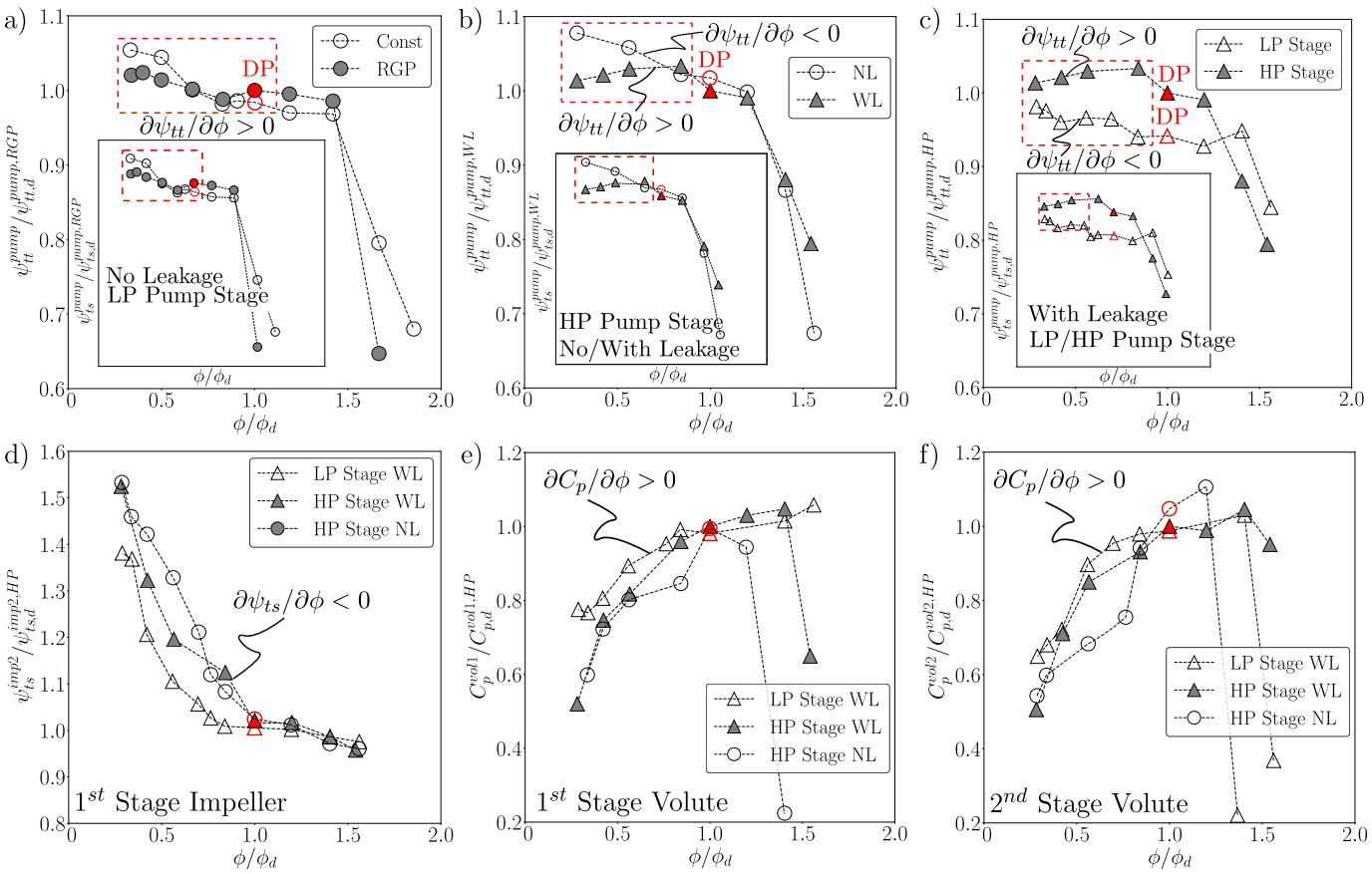

FIGURE 4: TOTAL-TO-TOTAL/STATIC PUMP HEAD RISE COEFFICIENT COMPARISON TO ASSESS A) COMPRESSIBILITY, B) LEAKAGE AND C) THERMODYNAMIC STATE EFFECTS. LEAKAGE AND PUMP STAGE COMPARISON OF D) TOTAL-TO-STATIC, 1^{ST} STAGE IMPELLER HEAD RISE COEFFICIENT AND STATIC PRESSURE RECOVERY COEFFICIENT FOR E) 1^{ST} STAGE AND F) 2^{ND} STAGE VOLUTES.

nearly identical due to the low kinetic energy of the flow, thus conclusions can be made by either metrics. The coefficients are normalised with the design value of the configuration of interest (see superscripts). The first comparison, aims to assess compressibility effects, thus the curves are derived using the baseline geometry and two different modelling approaches for the fluid: incompressible and RGP. In the low-pressure (LP) pump stage, hydrogen is in liquid form, however due to its compressibility and temperature rise, a density drop at the order of 10% across the pump was recorded [21]. In the high-pressure (HP) pump stage, hydrogen is in supercritical conditions and its density exhibits minor variations (less than 2%), thus the LP stage pump is only shown in Fig. 4a. Compressibility effects slightly enhance the head rise coefficient in the mid-to-high flow region due to

Copyright © 2025 by Rolls-Royce plc;
reuse license CC-BY 4.0

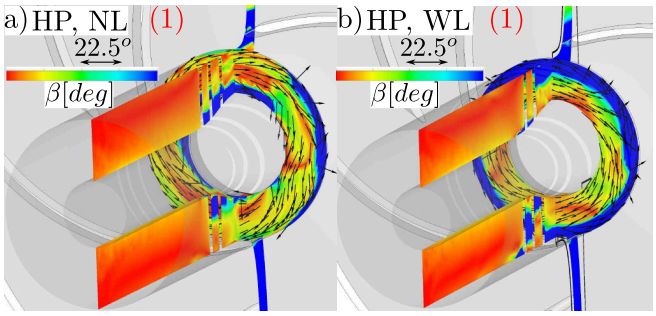

FIGURE 5: FLOW ANGLE CONTOURS AT 1^{ST} STAGE IMPELLER INLET A) WITHOUT AND B) WITH SHROUD LEAKAGE FLOWS AND ϕ/ϕ_d = 0.28.

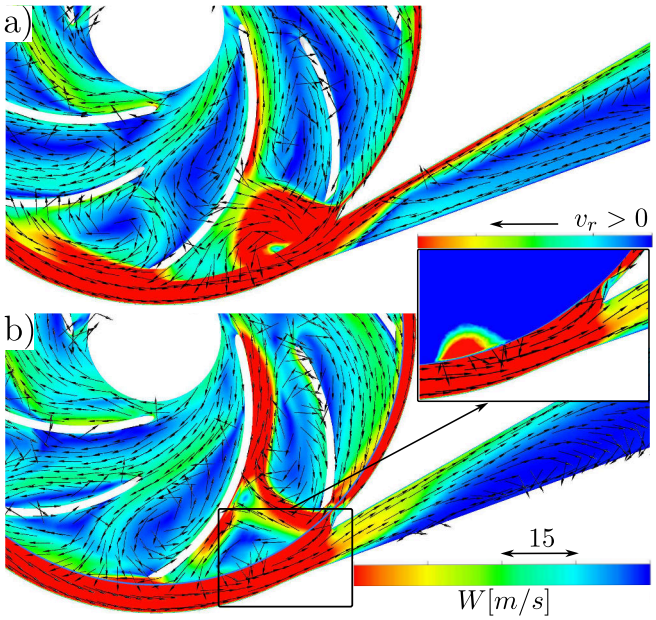

FIGURE 6: RELATIVE VELOCITY VECTORS AND CONTOURS NEAR THE VOLUTE TONGUE OF THE 1^{ST} STAGE IMPELLER AT ϕ/ϕ_d = 0.56 A) WITHOUT AND B) WITH CAVITIES.

the reduction in density. However, at low off-design flow rates, the beneficial effect of reduced density appears to be offset by the energy absorbed in fluid volumetric deformation, potentially alongside other contributing factors such as flow separations. Nonetheless, the overall slope remains unchanged. The total-to-static head rise coefficient exhibits identical trends, with the negative gradient indicating stable operation.

The impact of the leakage flows on the gradients of the ψ_{tt} and ψ_{ts} characteristics is assessed in the HP stage, as this exhibits the most unsteady behaviour (Fig. 4b). While in the higher flow rate region the two characteristics are almost identical, at the low flow-rate, off-design range there is a notable divergence between the two ψ_{tt} and ψ_{ts} curves. While the baseline, no-leakage (NL) configuration maintains a negative slope, the presence of leakage flows results in a peak after the design point, followed by a positive gradient. This indicates could potentially indicate a destabilising effect introduced by the leakage flows.

A comparison of the LP and HP stage with leakage flows is shown in Fig. 4c. As mentioned earlier, hydrogen is in liquid form in the LP stage and supercritical in the HP stage. Unlike the HP pump stage, the LP pump stage maintains a negative slope even in the very low flow rate operation which is also in concert with the corresponding total-to-static coefficient. The origins of the observed change in slope can be traced back to the destabilising effect of the volutes and adjacent ducting components. The impellers, regardless of compressibility, leakage or thermodynamic state effects, exhibit a consistent negative gradient slope throughout the entire flow rate range, as shown in Fig. 4d. The first and second stage volutes however, are characterised by a consistently positive static pressure coefficient gradient, except for the very high flow rates where the flow is highly separated. As the operation of the pump shifts towards the low mass flow region, the mismatch of the flow angles at the volute tongue precipitate progressively large separations. These manifest as reduced pressure coefficient values (see $\partial C_p/\partial\phi > 0$ region in Figs. 4e,f), thereby constituting the main destabilising components of the system.

One of the principal reasons underpinning the notably lower ψ_{tt} values in the presence of the leakage flows, observed in Fig. 4d, is the substantial change in the incoming flow angles at the impeller leading edge (LE) as the backwards-travelling flow through the shroud cavities mixes with the incoming main flow. The mass flow in the shroud cavities increases as a fraction of the overall pump mass flow as the latter is reduced, exacerbating this effect, as shown in Fig. 5. The dark-coloured ring forming around the shroud at the impeller inlet, reaches its maximum extent at low flow rates, substantially changing the incidence angle at the LE. The flow-field contours correspond to the HP pump stage and the lowest available flow rate setting, approximately $\phi/\phi_d = 0.28$.

The mild benefit exhibited by the full configuration in the volutes' pressure coefficients are linked with a suction effect near the volute tongue, which delays the onset of the separation at the volute. The mismatch between the impeller and the volute tongue, causes the nearby passage to stall, with flow travelling backwards from the volute tongue to the impeller inlet (Fig. 6a). This causes the flow to accelerate as it passes through the restricted unblocked region, thereby reducing the pressure sufficiently to create a suction effect in the shroud cavity which suppresses the extent of the local stalled flow, reducing the flow separation downstream the volute and the associated losses (Fig. 6b). This effect is more pronounced at higher flow rates and higher rotational speeds. At lower speeds, this beneficial suction effect progressively diminishes due to the lower velocities, resulting in higher losses compared to the baseline configuration.

4. UNSTEADY RESPONSE

4.1 MASS FLOW EFFECT

The pump is expected to operate at a wide range of off-design conditions, characterised by flow rates substantially lower than the design one. The unsteady response of the pump is by extension critical, as any high-energy fluctuations will propagate to the downstream components of the fuel system. To assess the intensity and evolution of the pump's unsteady performance, uRANS simulations are carried out at 3 different flow rates with the baseline configuration: $\phi/\phi_d = 0.84$, $\phi/\phi_d = 0.56$ and $\phi/\phi_d = 0.28$. Figure 7 shows the overall ψ_{tt}, first stage impeller ψ_{ts} and volute

Copyright © 2025 by Rolls-Royce plc;
reuse license CC-BY 4.0

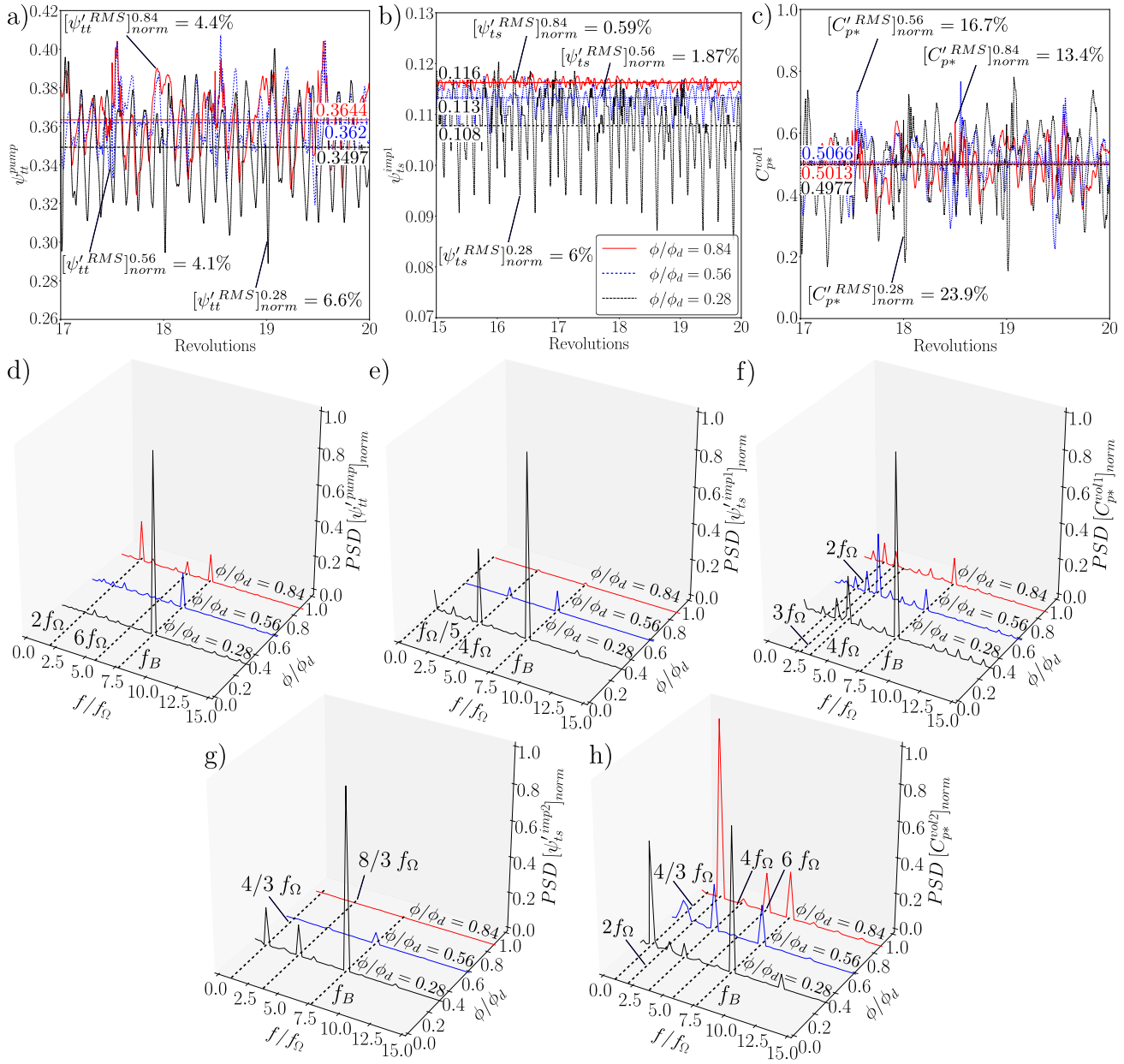

FIGURE 7: COMPARISON OF UNSTEADY ψ^{pump}_{tt}, ψ^{impl}_{ts} and C^{vol1}_{p*} AND FREQUENCY ANALYSIS OF THE CORRESPONDING FLUCTUATING COMPONENTS FOR THE HP PUMP WITHOUT LEAKAGE AT $\phi/\phi_d = 0.84$, $\phi/\phi_d = 0.56$ AND $\phi/\phi_d = 0.28$.

C_{p*} coefficients along with the corresponding frequency content obtained from fast Fourier transformation (FFT) of all components. The second stage impeller and volute are not shown as they exhibit similar behaviour and the main conclusions from the first stage analysis are transferable to the second stage. At the two highest ϕ/ϕ_d settings, the difference between time-averaged pump head coefficient is negligible. To assess the intensity of the oscillations, the root mean square (RMS) values of the fluctuating components are computed and normalised with the corresponding mean values. This indicates that at the two higher flow rates, their intensity is similar, equal to 4.4% and 4.1% of their time-averaged values respectively. At $\phi/\phi_d = 0.28$, the intensity of the fluctuations increases by approximately 50%, reaching 6.6%, with the amplitude of the peak values reaching 16.3% of the mean ψ_{tt} value. The power carried by the fluctuating components at the lowest flow rate is 11.2 times higher compared to mid-flow one. Focusing on the first stage impeller ψ_{ts} coefficient, it can be seen that the oscillatory behaviour of the impeller abruptly exacerbates at $\phi/\phi_d = 0.28$, with the corresponding RMS values increasing from 0.59% and 1.87% to 6%. This is further highlighted at the peak values, increasing from just 2.3% and 6.3% at the higher flow rates to 20.7%. This is also reflected on the signal power which is more than 9 times higher between the 2 lowest flow rates. The C_{p*} coefficient oscillations show noteworthy signs of unsteadiness throughout all flow rates, increasing progressively from 13.4% to 23.9%. The unsteadiness stems from the impeller-volute interaction and the onset of flow separation downstream the volute tongue, present at all operating points.

Copyright © 2025 by Rolls-Royce plc;
reuse license CC-BY 4.0

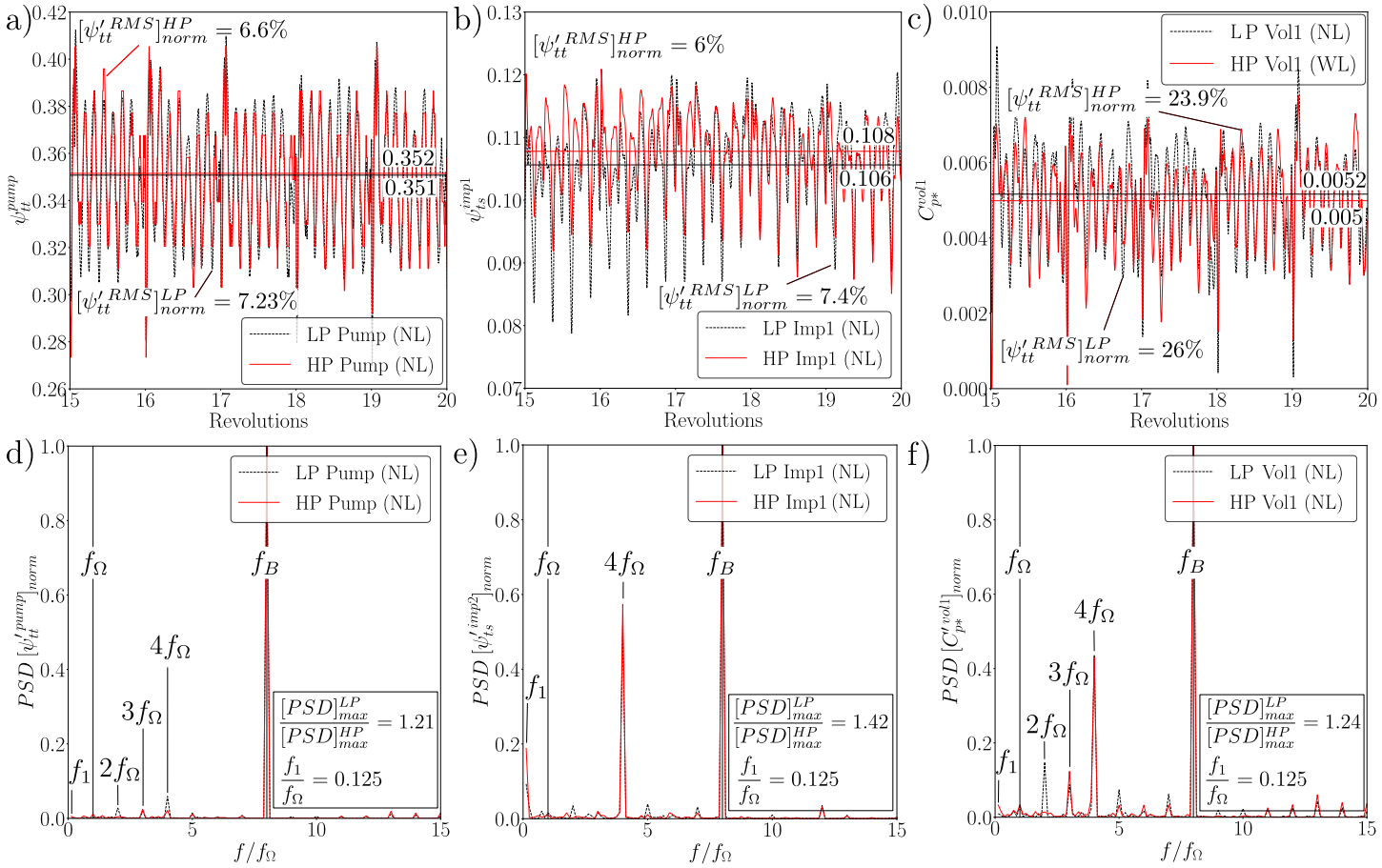

FIGURE 8: COMPARISON OF UNSTEADY ψ^{pump}_{tt}, ψ^{imp1}_{ts} and C^{vol1}_{p*} AND FREQUENCY ANALYSIS OF THE CORRESPONDING FLUCTUATING COMPONENTS BETWEEN THE LP AND HP PUMP WITHOUT CAVITIES AT $\phi/\phi_d = 0.28$.

The frequency content and the PSD of all components normalised with the corresponding highest power signal of all flow rates, are shown in Figs. 7d-h for the investigated ϕ/ϕ_d values. The frequencies are expressed as multiples of the rotor frequency, f_Ω, with $f_B = 8f_\Omega$ denoting the blade passing frequency. Observing all figures, it is evident that f_B, main/splitter blade passing frequency, $4f_\Omega$ as well as $2f_\Omega$ and $3f_\Omega$, are the dominant frequencies, all of which, are essentially harmonics. The $2f_\Omega$, present in the pump ψ_{tt} and C_{p*} coefficients of both volutes and downstream ducts, dissipates as the mass flow decreases and seems to be related to the dynamics of the volutes. On the contrary, the $3f_\Omega$ along with $4f_\Omega$ and $8f_\Omega$ increase drastically as flow reduces, with the latter two being the dominant frequencies in the first stage impeller and volute domains. This indicates a primarily impeller-driven unsteadiness along with a volute-impeller interacting phenomenon. In the second stage impeller and volute, a lower harmonic, with a frequency of $4/3f_\Omega$, dominates alongside the blade passing frequency, f_B, with the first emanating from the volute-diffusing duct domain.

4.2 THERMODYNAMIC STATE EFFECTS

To assess the potential impact of the thermodynamic state on the unsteady response of the pump, the LP and HP pump stages without leakage flows are compared at the lowest flow rate, equivalent to $\phi = 0.28\phi_d$, where hydrogen is in liquid and supercritical state, respectively (Fig. 8). In both cases, constant properties have been used for both fluids since for the LP stage, compressibility effects only introduced a slight deterioration in the head rise coefficient of the pump, without however changing the slope of neither the ψ^{pump}_{tt} nor the ψ^{pump}_{ts} (see Fig. 4a). In the HP pump, compressibility effects are negligible as the change in density does not exceed 2%. Both the HP and LP pump ψ_{tt} exhibit very similar mean and oscillatory characteristics. The peak fluctuating amplitude of the pump's ψ_{tt} reaches approximately 17.9% and 18.4% of the corresponding mean value for the LP and HP stages respectively. The RMS values of the fluctuating components indicate a higher-energy content in the LP stage, translating to an average fluctuating amplitude equal to 7.23% compared to 6.6% for the HP pump. This trend is consistent across the first stage impeller total-to-static head rise coefficient (Fig. 8b) and the modified static pressure coefficient of the volute (Fig. 8c). The second stage impeller and volute exhibit similar behaviour, with the ψ_{ts} RMS fluctuation being 8.13% and 8.9% for the LP and HP pump stages respectively, while the corresponding C_{p*} coefficients are close to 20%.

The transient signals are subsequently transformed from the time domain to the frequency domain to analyse the frequency content of the same components. The frequencies are again

Copyright © 2025 by Rolls-Royce plc;
reuse license CC-BY 4.0

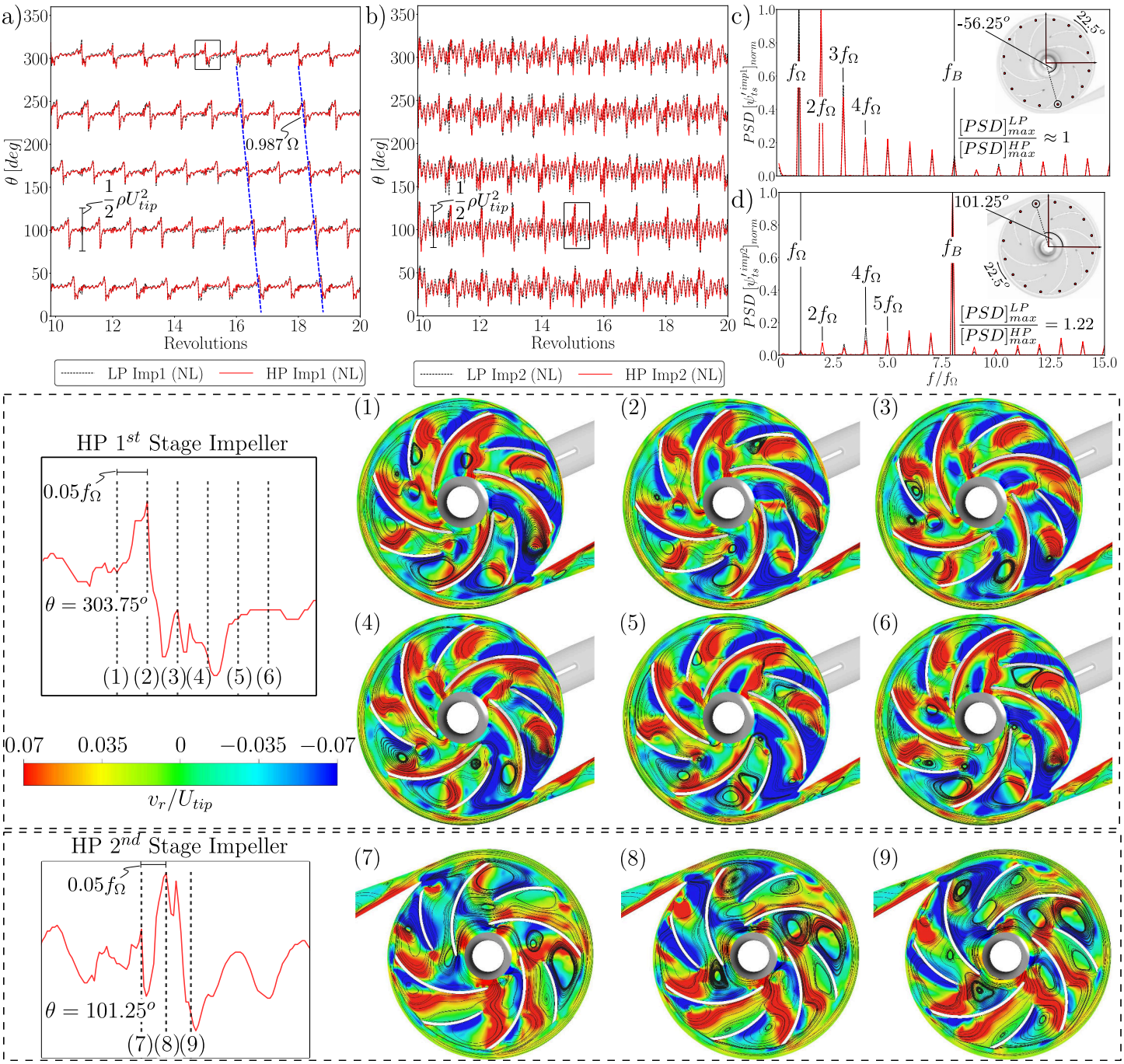

FIGURE 9: COMPARISON OF UNSTEADY STATIC PRESSURE SIGNALS NORMALISED WITH $1/2\ U_{tip}^2$ AT DIFFERENT CIRCUMFERENTIAL POSITIONS OF THE LP AND HP STAGES WITHOUT CAVITIES AND $\phi/\phi_d = 0.28$. FREQUENCY CONTENT OF THE SIGNALS CLOSE TO THE VOLUTE TONGUE AND RELATIVE VELOCITY SNAPSHOTS AT DIFFERENT TIME INSTANCES DURING SURGE-TYPE OF INSTABILITIES.

expressed as multiples of the rotor frequency with $f_1 = 0.125 f_\Omega$ representing the fundamental frequency. The power spectral density (PSD) corresponding to each frequency is then computed, providing a measure of the power contained in each frequency. The PSDs of the LP and HP pump/components are then normalised with their corresponding maximum values. The ratio of the maximum PSD values of each pump stage are also shown on the graphs for scaling purposes. Examining Figs. 8d,e,f, the principal frequencies lie within the $[0 - 15 f_\Omega]$ spectrum, with the highest-power ones being the blade passing frequency, f_B, along with $4 f_\Omega$, which essentially corresponds to blade passing frequency of the full or splitter blades. This indicates a strong impeller-volute interaction along with flow features associated with either the main or splitter blades. The contribution of the latter is substantial in the impellers/volutes but of second order in terms of the pump system. However as all the primary frequencies annotated on the plots are harmonics of the fundamental frequency, denoted with f_1, a degree of interaction between the

Copyright © 2025 by Rolls-Royce plc;
reuse license CC-BY 4.0

underlying mechanisms is expected, dampening or amplifying the primary frequencies observed in each component.

To determine the underlying mechanisms associated with the high-power frequencies and the unsteadiness in the impeller-volutes, pressure data along the first and second stage impeller outlet at different circumferential positions are extracted and normalised with $1/2\ \rho U_{tip}^2$ (Fig. 9a,b). The unsteady signals of the 1^{st} stage impeller resemble a mild surge-type behaviour, whereby a large pressure peak is followed by a sudden drop in pressure and a subsequent re-pressurisation region in a cyclic/repetitive pattern. A similar behaviour is observed in the 2^{nd} stage impeller, more evident at the $\theta = 101.25°$ position, close to the volute tongue, with the re-pressurisation phase being significantly more oscillatory. Tracing the high-pressure peaks along the circumference of the 1^{st} stage impeller, the surge phenomenon seems to not manifest instantaneously in the circumferential direction, but rather at an equivalent angular speed of about 0.987Ω. This is not observed in the second stage impeller. Transforming the pressure signals in the vicinity of the volute tongue in the frequency domain, supports these observations; contrary to the 2^{nd} stage impeller, where f_B essentially constitutes the primary frequency, the 1^{st} stage locally is governed by lower band frequencies $[f_\Omega - 4f_\Omega]$. These were identified also in the $\psi_{ts}^{\prime imp1}$ and $C_{p*}^{\prime vol1}$, with their contribution being much pronounced in the latter and negligible in the former, which was dominated by f_B (see Fig. 7f and Fig. 8e,f). This indicates that the flow-field locally is mainly driven by the impeller-volute interaction and the larger volume dynamics of the volute - 180° duct.

Radial velocity contours of the 1^{st} stage impeller normalised with the tip speed at various time instances, (1)-(6), during one of these cycles are shown in the middle of Fig. 9. Focusing on instance (1) and the full blade approaching the volute tongue, it can be seen that a stream of reverse flow convects backwards from the volute tongue, primarily through the fully stalled adjacent splitter blade. This is exacerbated as the passage further rotates towards the volute tongue, precipitating a large stalled flow region and blocking the outflow passage area (2). This results in a local pressure peak, as the pump must generate a higher head to overcome the resistance imposed by the stalled flow. As the main blade further rotates, the stalled flow mainly concentrates in a region close to the passage outlet, in-between the pressure side and the volute tongue, allowing the portion of the passage past the volute tongue to recover. This results in a pressure relief within the impeller. As the preceding splitter blade approaches the volute tongue and blockage starts forming due to the stalled flow stream emanating from the volute tongue, the reduced energy transfer of the splitter blade combined with its shorter length, instantly creates a large stream of flow travelling all the way to the passage inlet (4). This does not occur at full blades which due to the higher energy transfer, contain the stalled flow, sweeping it away shortly after. The flow reversal results in a further mild pressure drop, relieving locally the high pressure formed due to the blocked region. As the splitter blade rotates away from the volute tongue, the reverse flow stream gradually diminishes and only a small separated region remains. Depending on the blade, i.e. splitter of full, stalling seems to subside between 1/4 and 1/2 rotor revolutions, which translates to around $2f_\Omega - 4f_\Omega$, the dominant frequencies captured in Fig. 9c. The difference in the phase of the first stage impeller's mild surge cycles is most likely attributed to the difference between the stalling/unstalling frequency between the main and splitter blades, affecting how the pressure waves propagate circumferentially.

The mechanisms underlying the unsteadiness of the 2^{nd} stage impeller are similar. The main difference lies in the consistently less extended separated regions along both the main and the splitter blades as well as their formation primarily in the suction side of the full blades instead of the pressure side. This substantially ameliorates the extent of the stalled flow at the volute tongue and by extension the stalling characteristics it imposes on the main and splitter blade passage, which in the case of the former, is concentrated only in a small region at the pressure side of the full blade (7). This is also reflected on the milder pressure peak associated with the stalling of the main blade. As the splitter blade approaches the volute tongue, stalled flow blocks the entire outlet of the blade passage, resulting in a pressure peak, larger than the one caused by the main blade (8). Unlike the 1^{st} stage impeller, where a stream of flow travels back to the passage inlet when the stalled splitter blades pass near the volute tongue, this phenomenon does not occur in the 2^{nd} stage impeller (9). This is also reflected in the lower PSD at $4f_\Omega$, which was predominantly related to the more heavily stalled splitter blades of the first stage impeller. In the second stage, the stalling characteristics between the main and splitter blades are more similar and localised, diminishing shorty after the volute tongue, which is reflected on the high power frequency content at f_B and the lower power frequency content in the lower frequency range.

4.3 LEAKAGE FLOW EFFECTS

A similar analysis is conducted to identify the implications of leakage flows on the unsteady response of the pump at low flow operation. For the comparison, the HP pump is chosen, where the flow is incompressible. The simulations are again carried out at the lowest flow rate, i.e. $\phi/\phi_d = 0.28$, using the shroud leakage-only configuration, since the interaction of the hub and motor cavities is insignificant compared to the impeller shroud cavities [21]. Figure 10a-c shows the pump ψ_{tt} as well as 1^{st} stage impeller ψ_{ts} and volute C_{p*} coefficients obtained transiently, over a window of 5 revolutions. The time-averaged pump head rise coefficient of the shroud leakage-only configuration shows a penalty of approximately 2.5% in the overall pump performance and 10.2% in the 1^{st} stage impeller (18.6% for the 2^{nd}). As described earlier, this is mainly due to the change in the incidence angle induced by the mixing of the leakage and the core flow. The beneficial effect of the leakage flows observed in the steady-state simulations (see Fig. 4) is also evident here, showing an increase in the modified static pressure coefficient of both volutes (1^{st} stage shown here). Despite the overall performance penalty introduced by the shroud leakage cavities, the shroud configuration pump exhibits substantially lower intensity fluctuations, the RMS value of which, is approximately 44.1% lower than the baseline's ones. In terms of peak fluctuating components, the peaks of ψ_{tt} diminish from 18/4% to 10.3%. The intensity of the impellers' fluctuations slightly increase in the first stage due to the presence of the leakage flows, from 6%

Copyright © 2025 by Rolls-Royce plc;
reuse license CC-BY 4.0

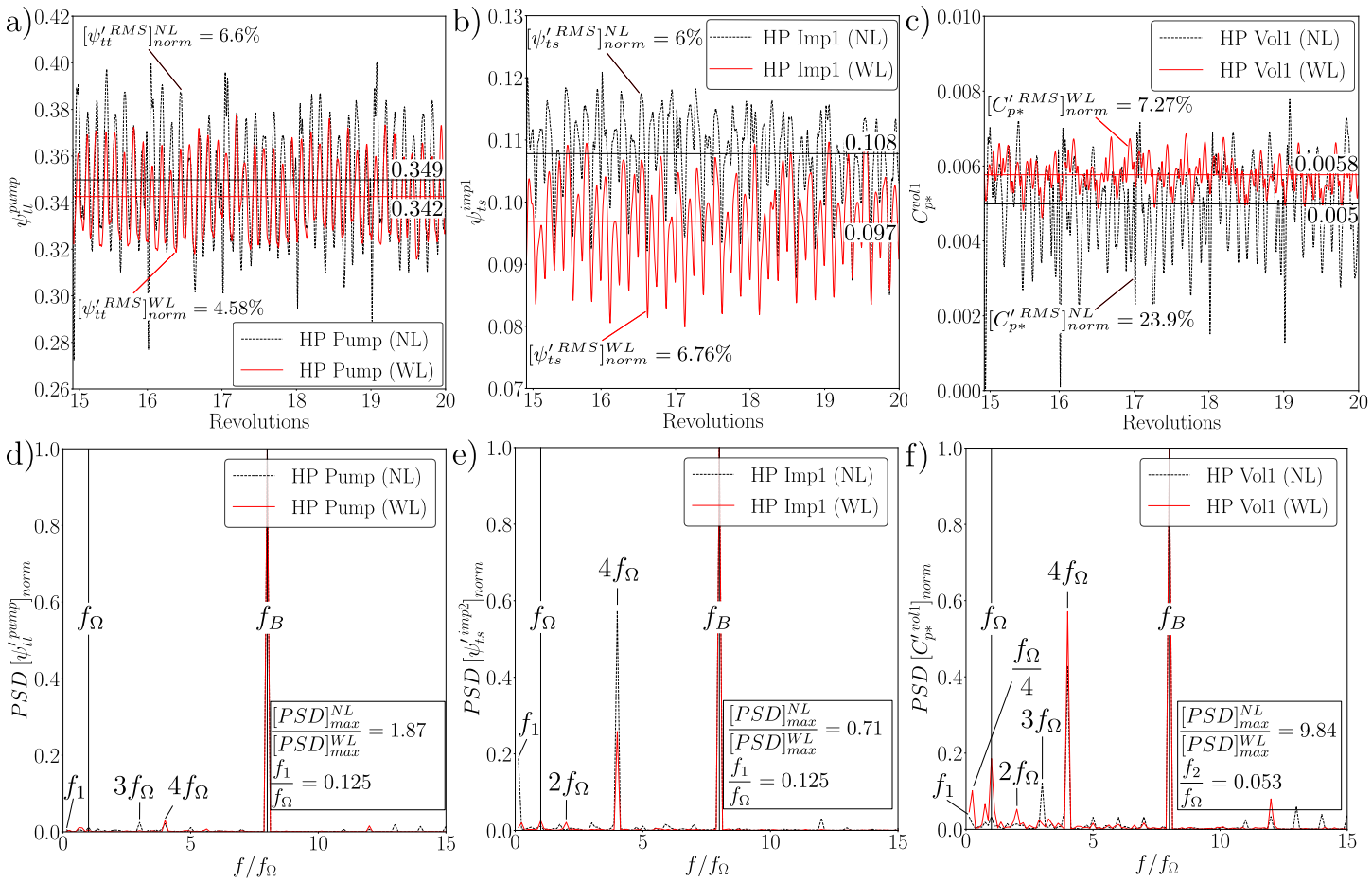

FIGURE 10: COMPARISON OF UNSTEADY ψ_{tt}^{pump}, ψ_{ts}^{imp1} and C_{p*}^{vol1} AND FREQUENCY ANALYSIS OF THE CORRESPONDING FLUCTUATING COMPONENTS BETWEEN THE HP STAGE PUMP WITH AND WITHOUT CAVITIES.

to 6.7% and slightly reduce in the second, from 8.2% to 7.2%. The peak amplitude values are also similar and are in the range [14.1% – 13.1%] and [16.3% – 16.8%] for the first and send stage impellers, respectively. The unsteadiness of both impellers is however substantially offset by the reduction in the average fluctuation amplitude of both volutes' by approximately three times, which is sufficiently high to dampen the energy of the oscillations of the entire pump.

In terms of the fluctuations' frequency content, the pump head rise coefficient does not indicate any noteworthy differences, with the dominant frequency being the blade passing frequency. Its power is 1.87 times higher for the baseline configuration which is also reflected in the aforementioned RMS values of the fluctuating components in Fig.11d. In the 1^{st} impeller (Fig.11e), the contribution of the $4f_\Omega$ frequency decreases (as a fraction) notably, while in the volute there is an increased contribution from lower frequency signals in the range $[f_1 - 4f_\Omega]$; in the previous section, these were linked to the volute and the stalling/unstalling frequency of the blades. It should be noted that in the volute, the power of the signals corresponding to the baseline configuration are 9.84 higher than the shroud cavity configuration (Fig.11f).

Figures 11a,b show the normalised pressure signals obtained at different circumferential locations at the outlet of the 1^{st} and 2^{nd} stage impeller. Contrary to the surge-type behaviour of the baseline model (discussed in the previous paragraph), the leakage configuration does not exhibit any signs of cyclic pattern in neither of the impellers. Moving circumferentially towards the volute tongue (303.75^o and 101.25^o for the 1^{st} and 2^{nd} stage respectively), the energy of the leakage configuration's pressure signals increases progressively. In terms of frequencies (Figs. 11c,d), the presence of the leakage flows seems to substantially dampen the high-power signals in the lower $[f_1 - 4f_\Omega]$ frequency range, with most of the power being associated with the blade passing frequency. It should be highlighted that the peak PSD values corresponding to the impellers of the baseline configuration are 1.44 and 3.96 times higher, highlighting the favourable impact of the shroud cavities near the volute tongue, which was also observed in the steady-state simulations.

Flow-field snapshots at different time instances are shown in Fig. 11 for the 1^{st} and 2^{nd} stage impellers of the HP pump with shroud leakages. The snapshots of the 1^{st} stage impeller are captured close to 2 high-pressure and low-pressure peak instances. The low flow-rate, off-design operation alongside the change in incidence angle caused by the mixing of the shroud leakage and main flow, result in high negative incidence angles. This causes flow separation at the suction side of the splitter blades, forming

Copyright © 2025 by Rolls-Royce plc;
reuse license CC-BY 4.0

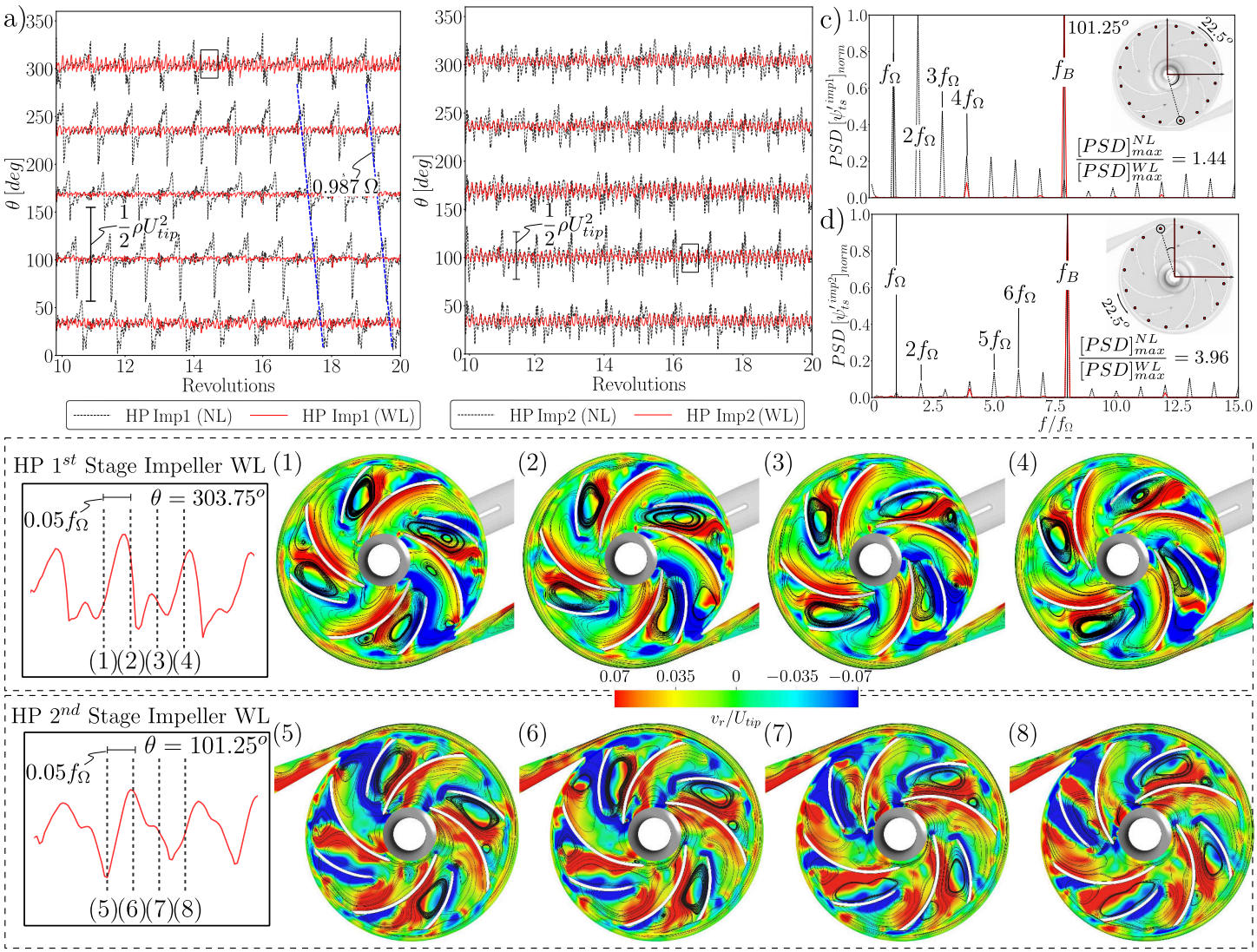

FIGURE 11: UNSTEADY STATIC PRESSURE SIGNALS COMPARISON AT ϕ/ϕ_d = 0.28 NORMALISED WITH 1/2 U_{tip}^2 AT DIFFERENT CIRCUMFERENTIAL POSITIONS OF THE HP PUMP STAGE WITH AND WITHOUT SHROUD LEAKAGE. FREQUENCY CONTENT NEAR THE VOLUTE TONGUE AND RELATIVE VELOCITY SNAPSHOTS AT DIFFERENT TIME INSTANCES FOR THE SHROUD LEAKAGE CONFIGURATION.

counter-clockwise rotating vortices in half of the blade passages. The first time snapshot (1), is captured in the proximity of the first, low-peak pressure point. As the splitter blade approaches the volute tongue, the stalled flow-induced blockage precipitates extensive flow reversal on the pressure side of the splitter blade. This enables a stream of fluid to travel backwards to the passage inlet, affecting the matching between the impeller and the volute as well as the local pressure distribution. The presence of the vortex and the increase in static pressure near the volute creates a small region of stalled flow in the preceding passage. As the preceding passage approaches the volute tongue, the stalled flow region increases, blocking the passage which in turn translates to increased pressure output (2). The stalled region further increases, creating flow reversal mainly at the suction side of the splitter blade, as the pressure side starts to unstall, causing a less sudden pressure drop (3). The stalled flow subsequently reaches its maximum size, leading to another increase in pressure, as the main blade is able to sustain the required head to prevent full flow reversal. The stall region on the main blade is localised and confined on the pressure side within between the middle of the chord and the TE. This is in contrast to the splitter blades which stall due to high negative incidence from the suction side and due to stalling from the pressure side. The second stage impeller (5) - (8) exhibits a similar stalling pattern; the lowest pressure point corresponds to the discharge of the stalled flow from the volute to the passage inlet, and peaks when the stalled flow blocks a large fraction of the passage, requiring the impeller to produce additional head output to overcome the low-momentum stalled flow. Compared to the baseline configuration, in both impeller stages the extent of the separation regions is notably smaller and dissipate at a much faster rate. This benefit is induced by the suction effect in the shroud cavity, which partially dissolves the stall cell in the volute tongue, ameliorating its detrimental implications. The faster recovery of all blades and particularly the more heav-

Copyright © 2025 by Rolls-Royce plc;
reuse license CC-BY 4.0

ily stalled splitter blades, increases the overall frequency of the phenomenon, which is also reflected on the weaker power signals in the lower frequency range.

5. SUMMARY AND CONCLUSIONS

The effect of mass flow, compressibility, leakage flows and thermodynamic state on the stability and transient response of a representative LH2 fuel system pump for aircraft engine applications is carried out by means of RANS and uRANS simulations. This is achieved by analysing the response of three different model configurations with partial, full and without cavities combined with 2 different fluid modelling approaches i.e. RGP and constant properties. A stability assessment analysis is initially performed at an overall pump and individual component level by comparing the slopes of the ψ_{tt}^{pump}, ψ_{ts}^{imp} and C_p^{vol} curves of the different subcomponents. Compressibility effects penalise ψ_{tt}^{pump}, reducing the ψ_{tt}^{pump} gradient in the lower ϕ region, without however changing its sign, indicating minor implications on the stability of the system. Both leakage and thermodynamic state effects however, change the ψ_{tt}^{pump} slope and are therefore analysed in more detail. The positive C_p slope of the volutes indicates that they are the destabilising components of the system.

Lowering the flow rate of the pump up to $\phi/\phi_d = 0.56$ does not display any noteworthy variations in the intensity nor the peaks of the unsteadiness. At $\phi/\phi_d = 0.28$ however, a 50% increase in the intensity of the fluctuations is recorded with the peak amplitude reaching 16.3% of the mean value. The thermodynamic state, i.e. liquid or supercritical in terms of time-averaged performance does not introduce any noteworthy changes, with the LP pump (liquid) exhibiting slightly higher oscillations. The RMS values of the pump's ψ_{tt} fluctuating components are at the order of 7.23% of the corresponding average values, with peak amplitude of up to 18.4% for the HP pump stage. Both impellers undergo a cyclic, surge-type of event, whereby stalled flow manifests and progressively increases as the passage approaches the volute tongue, blocking the passage exit. This causes heavy stalling in the splitter blades and milder in the full blades, with the disturbances travelling circumferentially at a speed of 98.7% Ω. This creates a peak pressure followed by a sudden drop, coinciding with the development of fully reverse flow in the splitter and partial in the full blades. In the 2^{nd} stage impeller, the flow reversal is more localised in the splitter blades but the energy of the fluctuations is higher due to the higher pressure in the impeller.

As expected, the presence of leakage flows penalises the time-averaged pump by 2% however the RMS fluctuations of the pump decrease by 44.1%. This is linked to the favourable suction effect induced by the shroud leakage flow which partially breaks the stall cell near the volute, decreasing the RMS fluctuations by almost 3 times compared to the baseline configuration. This drastically reduces the extent and recovery rate of the stalled blades, which is also reflected on the frequencies content, dampening the low frequency signals which were associated with the impeller-volute interaction and recovery rate of particularly the splitter blades. Beyond the analysis of the unsteady flow physics and stability characteristics of a representative pump configuration provided herein, the reported normalised metrics quantifying the unsteadiness of the pump are expected to be broadly transferable to analogous hydrogen pump designs. These may offer valuable insights for higher-level studies across diverse pump designs beyond the specific case investigated here. Finally, the paper provides a methodology for analysing the stability and unsteady response of future LH2 pumps, covering thermodynamic, compressibility and leakage flow modelling aspects, which are also expected to be relevant for other LH2 pump architectures.

ACKNOWLEDGMENTS

The authors would like to thank ATI/iUK for funding this work through UKRI, project LH2GT, with Reference No. 10039770 and Rolls-Royce plc. for their support and allowing its publication.

REFERENCES

[1] Adler, E. J., and Martins, J. R. R. A., 2023, "Hydrogen-powered aircraft: Fundamental concepts, key technologies, and environmental impacts," *Prog. Aerosp. Sci.,* **141**, p. 100922 Special Issue on Green Aviation.

[2] Petrescu, R. V. V., Machín, A., Fontánez, K., Arango, J. C., Márquez, F. M., and Petrescu, F. I. T., 2020, "Hydrogen for aircraft power and propulsion," *Int. J. Hydrogen Energy,* **45**(41), pp. 20740–20764.

[3] Smith, J. R., and Mastorakos, E., 2024, "An energy systems model of large commercial liquid hydrogen aircraft in a low-carbon future," *Int. J. Hydrogen Energy,* **52**, pp. 633–654.

[4] Prewitz, M., Bardenhagen, A., and Beck, R., 2020, "Hydrogen as the fuel of the future in aircrafts – challenges and opportunities," *Int. J. Hydrogen Energy,* **45**(46), pp. 25378–25385.

[5] Brewer, G. D., 2017, *Hydrogen Aircraft Technology* Routledge.

[6] Ebrahimi, A., Rolt, A., Jafari, S., and Anton, J. H., 2024, "A review on liquid hydrogen fuel systems in aircraft applications for gas turbine engines," *Int. J. Hydrogen Energy,* **91**, pp. 88–105.

[7] Rompokos, P., Kyritsis, V., Mourouzidis, C., and Roumeliotis, I., 2024, "Assessment of a liquid hydrogen conditioning system for retrofitting on kerosene designed turbofan," In Proceedings of ASME Turbo Expo 2024: Power for Land, Sea, and Air, Vol. 1: Aircraft Engine, p. V001T01A009.

[8] Crease, G., Lyda, R., Park, J., and Minick, A., 1999, "Design and test results of an advanced liquid hydrogen turbopump," In Proceedings of the 35th Joint Propulsion Conference and Exhibit.

[9] Paniagua, G., Lavagnoli, S., Verstraete, T., Mahmoudi, W., and Benamara, T., 2013, "Aero-design of transonic lh2 and lox contra rotating turbopumps in an expander rocket engine," *International Journal of Numerical Methods for Heat and Fluid Flow,* **23**(4), pp. 575–587.

[10] Kanda, T., 2013, "Conceptual study of throttled operation of rocket engine turbopump," *Transactions of the Japan Society for Aeronautical and Space Sciences,* **56**(1), pp. 49–60.

[11] Day, I. J., 2015, "Stall, surge, and 75 years of research," *Journal of Turbomachinery,* **138**(1), 10, p. 011001.

Copyright © 2025 by Rolls-Royce plc;
reuse license CC-BY 4.0

[12] Spakovszky, Z. S., and Roduner, C. H., 2009, "Spike and modal stall inception in an advanced turbocharger centrifugal compressor," *Journal of Turbomachinery,* **131**(3), 04, p. 031012.

[13] Everitt, J. N., and Spakovszky, Z. S., 2012, "An investigation of stall inception in centrifugal compressor vaned diffuser1," *Journal of Turbomachinery,* **135**(1), 11, p. 011025.

[14] Van den Braembussche, R., 2020, *Design and Analysis of Centrifugal Compressors* ASME Press, 01.

[15] Frigne, P., and Van Den Braembussche, R., 1984, "Distinction between different types of impeller and diffuser rotating stall in a centrifugal compressor with vaneless diffuser," *Journal of Engineering for Gas Turbines and Power,* **106**(2), 04, pp. 468–474.

[16] Shim, H., and Kim, K.-Y., 2020, "Relationship between flow instability and performance of a centrifugal pump with a volute," *Journal of Fluids Engineering,* **142**(11), August, p. 111208.

[17] Wang, H., and Tsukamoto, H., 2003, "Experimental and numerical study of unsteady flow in a diffuser pump at off-design conditions," *Journal of Fluids Engineering,* **125**(5), October, pp. 767–778.

[18] Gao, B., Guo, P., Zhang, N., Li, Z., and Yang, M., 2017, "Unsteady pressure pulsation measurements and analysis of a low specific speed centrifugal pump," *Journal of Fluids Engineering,* **139**(7), April, p. 071101.

[19] Kaupert, K. A., and Staubli, T., 1999, "The unsteady pressure field in a high specific speed centrifugal pump impeller—part i: Influence of the volute," *Journal of Fluids Engineering,* **121**(3), September, pp. 621–626.

[20] Casimir, N., Zhu, X., Hundshagen, M., Ludwig, G., and Skoda, R., 2020, "Numerical study of rotor–stator interaction of a centrifugal pump at part load with special emphasis on unsteady blade load," *Journal of Fluids Engineering,* **142**(8), April, p. 081203.

[21] Lamprakis, D., Rajendran, D. J., Santhanakrishnan, M., Coskun, S., Roumeliotis, I., Pachidis, V., and Yates, M., 2024, "On leakage flows in a liquid hydrogen multistage pump for aircraft engine applications," *Journal of Engineering for Gas Turbines and Power,* **147**(5), 11, p. 051015.

[22] Lemmon, E. W., Bell, I. H., Huber, M. L., and McLinden, M. O., 2018, NIST Standard Reference Database 23: Reference Fluid Thermodynamic and Transport Properties—REFPROP, Version 10.0.

[23] Kulkarni, S., Beach, T. A., and Skoch, G. J., 2013, "Computational study of the cc3 impeller and vaneless diffuser experiment," In Proceedings of the 49th AIAA/ASME/SAE/ASEE Joint Propulsion Conference.

[24] Blumenthal, R. F., and Kelecy, F. J., 2021, "Numerical predictions of cavitating flow within a liquid hydrogen inducer," In Proceedings of ASME Turbo Expo 2021: Power for Land, Sea, and Air, Vol. 2C: Turbomachinery — Design Methods and CFD Modeling for Turbomachinery; Ducts, Noise, and Component Interactions, p. V02CT34A035.

[25] Shin, K., and Hammond, J., 2008, *Fundamentals of Signal Processing for Sound and Vibration Engineers* John Wiley & Sons.

[26] Lathi, B., 2010, *Modern Digital and Analog Communication Systems* Oxford University Press.

Copyright © 2025 by Rolls-Royce plc;
reuse license CC-BY 4.0

https://dspace.org/

On the unsteady behaviour of a liquid hydrogen fuel system pump for aircraft engine applications

Lamprakis, Dimitrios; Rajendran, David John; Yates, Martin; Roumeliotis, Ioannis; Pachidis, Vassilios

2025-06-16
American Society of Mechanical Engineers (ASME)
https://doi.org/10.1115/gt2025-153718
Lamprakis D, Rajendran DJ, Yates M, et al., (2025) On the unsteady behaviour of a liquid hydrogen fuel system pump for aircraft engine applications. In: ASME Turbo Expo 2025: Turbomachinery Technical Conference and Exposition, 16-20 June 2025, Memphis, USA, Volume 4: Controls, Diagnostics & Instrumentation; Cycle Innovations; Education; Electric Power. Paper number GT2025-153718

Downloaded from a DSpace repository. https://dspace.org/